Large scales in the developing mixing layer

By F. K. BROWAND AND P. D. WEIDMAN

Division of Engineering and Applied Mechanics,
University of Southern California, Los Angeles

A new experimental technique is described for the study of the interactions between the large-scale vortical features in the two-dimensional mixing layer. Detector probes above and below the mixing layer are used to monitor the large-scale structure. Conditional sampling is performed in a moderate Reynolds number developing flow, by using phase and amplitude information from these detector probes. It is shown that significant Reynolds-stress production is associated with the pairing interaction in which two vortical structures combine to form a single, larger vortical structure.

1. Introduction

In the past few years, a decidedly different approach has been applied to the experimental study of turbulent flows. The new experimental technique reflects a philosophical change in the conception of turbulence. As viewed today, turbulence is not as disorganized as people have previously believed. The beginnings of this conceptual change are hard to pin-point for, of course, turbulence has always been subject to a broad spectrum of interpretation, but the visual observations of boundary-sublayer structure performed by Kline *et al.* (1967) and Kim, Kline & Reynolds (1971) contributed significantly to a general feeling that organized motions are important locally.

The description of the large-scale motions existing in free turbulent flow dates back, at least, to Townsend (1956). Recent observations of the turbulent mixing layer show the large-scale structure to consist of vortical lumps or, simply, vortices aligned across the flow. Apparently, these vortices are formed by a redistribution of mean flow vorticity: there is little stretching of vortex lines involved. At mixing-layer Reynolds numbers between 300 and 1000 (based upon velocity difference and maximum slope thickness), Winant & Browand (1974) have shown that an interaction takes place whereby two neighbouring vortices coalesce to form a single, larger vortex. The spacing between vortices is then roughly doubled. Continuous repetition of this 'pairing' process is responsible for the entrainment of surrounding fluid, and controls the growth of the mixing layer. Because pairing is an instability, initiated by irregularities in vortex spacing and strength, the interaction is not fixed in space. At a given downstream location one sees, at different times, the passage of unpaired vortices, vortices in various stages of pairing, and vortices which have completed pairing. (This spatial and temporal 'jitter', when averaged over long times, accounts for the linear growth of the mixing layer.)
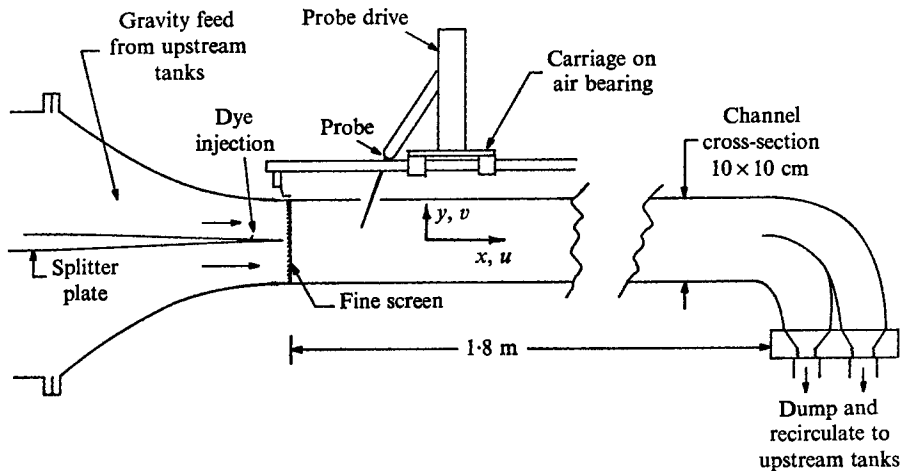
FIGURE 1. Schematic diagram of test apparatus.

Brown & Roshko (1971, 1974) have observed similar vortical structure at Reynolds numbers of order 250000. Thus certain qualitative features of the large-scale structure appear to be independent of Reynolds number over a large range, at least a partial justification for our present preoccupation with the relatively lower Reynolds number flow.

Historically, observation and verification of structure in turbulent flows has been largely based upon visual observations. With the digital computer however, the present-day researcher has the capability to search large data sets and perform the ensemble averaging necessary to isolate randomly occurring, but (locally) organized, events. The present experiment describes one way in which information on the large-scale structure in the developing mixing layer can be obtained. Use is made of two detector probes, one above and one below, which continually monitor the states of the mixing layer. The condition (or origin in time marking an 'event') necessary to form the ensemble is not based upon the detection of the turbulent/non-turbulent interface but, rather, is based upon the passage of the large-scale structure itself. Two flow states are unambiguously defined, and the local flow fields associated with these states are examined. It is hoped that the method can be extended to include an entire sequence of intermediate states.

2. Experimental set-up

The work described here was undertaken to provide more detailed information about the velocity field in the turbulent mixing layer studied by Winant & Browand (1974). Measurements were performed in the water channel shown schematically in figure 1. The mixing layer was formed downstream from a splitter plate dividing two streams having velocities of 5·1 cm/s and 2·1 cm/s, respectively. The measurement station was located 15 cm downstream from the origin, and marks the beginning of the region of linear mixing-layer growth. The
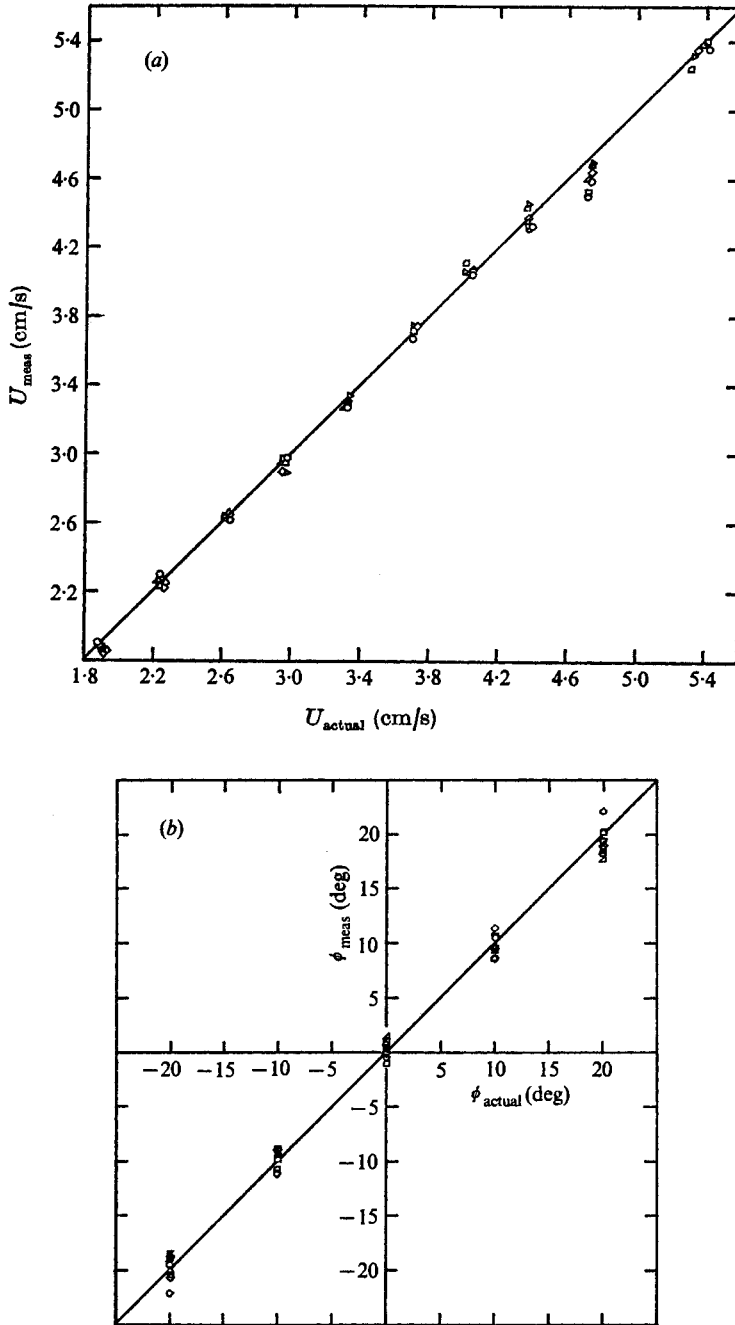
FIGURE 2. Split-film calibration. (*a*) Velocity magnitude. (*b*) Velocity direction.

maximum slope thickness, defined as $\Delta U/(dU/dy)_{\max}$, was $1\cdot05 \pm 0\cdot05$ cm; the momentum thickness was $0\cdot20$ cm; and the maximum mean shear was approximately $2\cdot9$ s^{-1}. The local Reynolds number based on velocity difference and maximum slope thickness, $\Delta Uh/\nu$, was about 300; the speed ratio was $\Delta U/\overline{U} = 0\cdot84$. The turbulence level in the free stream was approximately $0\cdot5$ %.

Data consisted of measurements of the instantaneous longitudinal and vertical velocities u and v at 13 vertical positions in the mixing layer. Velocities were determined using a Thermo-Systems split-film sensor, operated at constant temperature. Instantaneous voltages from the split-film sensor and the two detector hot films were recorded on magnetic tape. All data manipulation, including calibration, was performed on a digital computer. The time-averaged results presented later were calculated on two separate occasions starting with the analog tape and using completely different procedures and programs. The results were identical. The data were checked for trends (non-stationarity) and were smoothed to remove any possible instrument drift which might contribute to spurious r.m.s. results. No trends or instrument drift were detected.

The split-film sensor consists of two separate semi-cylindrical platinum coatings deposited on a quartz rod $0\cdot152$ mm in diameter. The half-films were operated in separate matched feedback loops which maintained the films at equal temperatures (as nearly equal as possible). The power needed to heat *both* halves of the cylindrical sensor to some fixed temperature in the fluid stream should be little different from the power required to heat a single cylindrical sensor. Thus the sum of the squares of the voltages from the two half-films is practically independent of the direction of the velocity (in the plane normal to the axis of the cylinder) and determines the magnitude of the instantaneous velocity vector. The difference in the squares of the voltages is sensitive to both velocity direction and velocity magnitude. The flow angle was determined by a polynomial fit of the sums and differences of the squares, using calibration data. (To our knowledge, no adequate theory is available which correctly describes the operation of the split film.) Figures 2(a) and (b) show the accuracy obtained for $U = (u^2+v^2)^{\frac{1}{2}}$ and $\phi = \tan^{-1}(v/u)$, for a typical calibration. The standard deviation in U is about $\pm 0\cdot02\Delta U$, and in ϕ about $\pm 1\cdot0°$. Greater familiarity and use will undoubtedly improve the accuracy.

3. Conditional sampling

Figures 3(a) and (b) (plates 1 and 2) show examples of the low-pass filtered (10 Hz cut-off) instantaneous signals from the two detector probes together with photographs of the flow. Dye was introduced upstream and marks the fluid having large vorticity. The vertical bars on the time traces indicate the time of the photograph. In figure 3(a), a pairing has already occurred (although the two original portions can still be distinguished). The detector-probe signals are almost exactly out of phase, as would be appropriate for the passage of a single vortical lump convected with the mean speed. In figure 3(b), a pairing is in progress and is accompanied by a repeatable, characteristic form of the detector-

probe signals. There is a strong phase shift, with the minimum signal on the lower trace lagging the maximum on the upper trace by about 50°.

Two states could be chosen for study, corresponding closely to the examples just discussed. State I was achieved when the detector signals satisfied the following conditions.

(a) Relative maxima and minima of the signals exceeded an amplitude threshold, 1·2 r.m.s.

(b) Wave forms possessed symmetry: each half-period did not exceed the previous half-period by more than 16 % of the total period.

(c) The algebraic sum of the reference signals was always less than 1·2 r.m.s.

These conditions served to isolate those intervals in time corresponding to the passage of vortices which had recently completed a pairing.

State II was achieved under the following conditions.

(a) Relative maxima and minima of the signals exceeded an amplitude threshold, 1·2 r.m.s.

(b) A phase lag of the proper sign (as illustrated in figure 2b) and of magnitude $50 \pm 15°$ existed between the reference signals.

In this case, the criteria corresponded to an intermediate state in the pairing process.

The conditions characterizing either state are, to some degree, subjective. In fact, this is true of any condition or set of conditions which might be applied; the subjective nature of the choice is a universal problem for those involved with conditional sampling. In our case, the above rules were justifiable directly in terms of the visualizations of the flow and did isolate interesting alternative flow states. Hopefully, however, the procedure can be generalized and extended.

The ensembles for states I and II were formed by marking an origin in time when the proper criteria were met, and then sampling 15 time steps earlier and 14 time steps later. The total time interval (30 samples), corresponding to 1·2 s, was slightly larger than the time required for paired vortices to pass the probe. The entire data record was 52 min in length. The ensemble corresponding to state I occupied 2 % of the total time record, and that corresponding to state II occupied 4 % of the record. This does *not* mean that events resembling state I and state II occur that infrequently; it only means that we have chosen a small fraction of those events: the ones which satisfy particular, stringent requirements on the amplitude and phase at a fixed point in space. Relaxing those requirements results in a greater number of ensemble members, but at the expense of 'blurring the image'. The question was resolved by choosing the sampling conditions to give the smallest sample which still yielded statistically smooth averages. (Even so, the sample for state I is probably too small, and statistical fluctuations are evident in some of the conditioned results.)
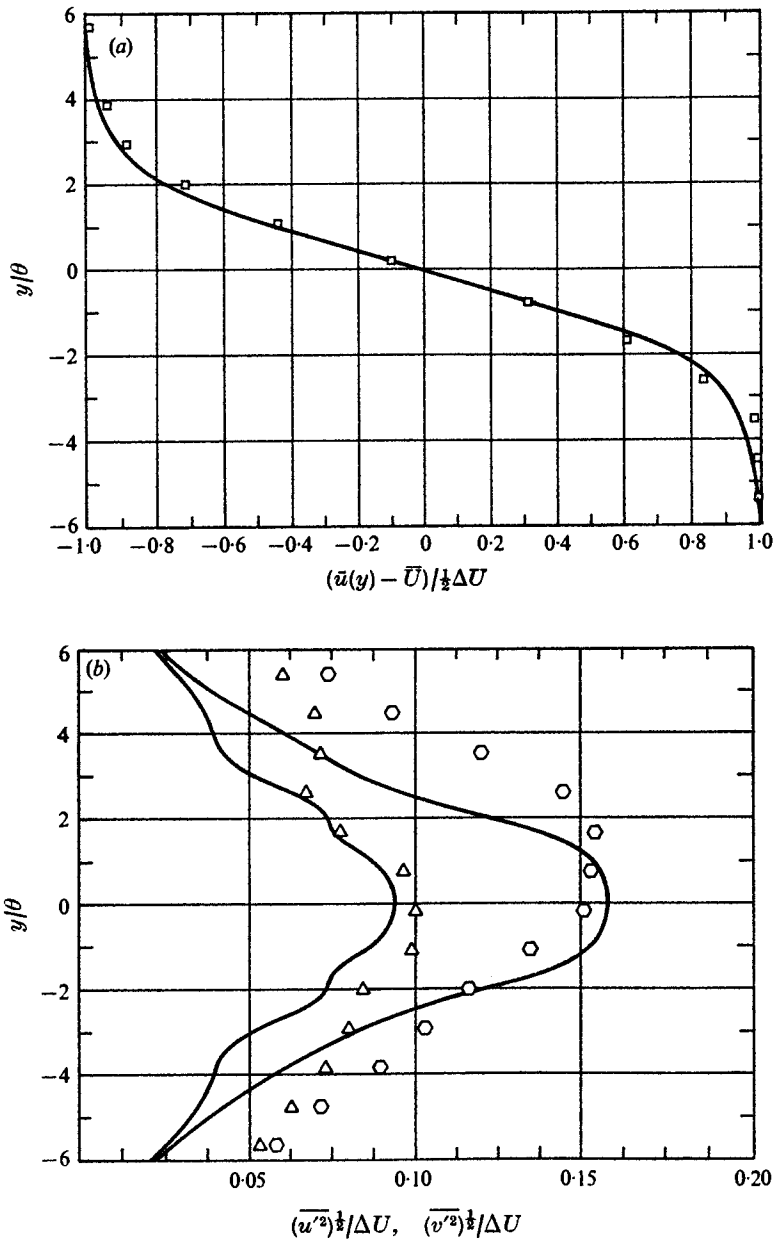
FIGURE 4. (a) Time-averaged longitudinal velocity (squares); ——, flow model using Stuart vortices. (b) R.m.s. velocity fluctuations. $\triangle$, longitudinal; $\bigcirc$, vertical; ——, results from flow model using Stuart vortices.
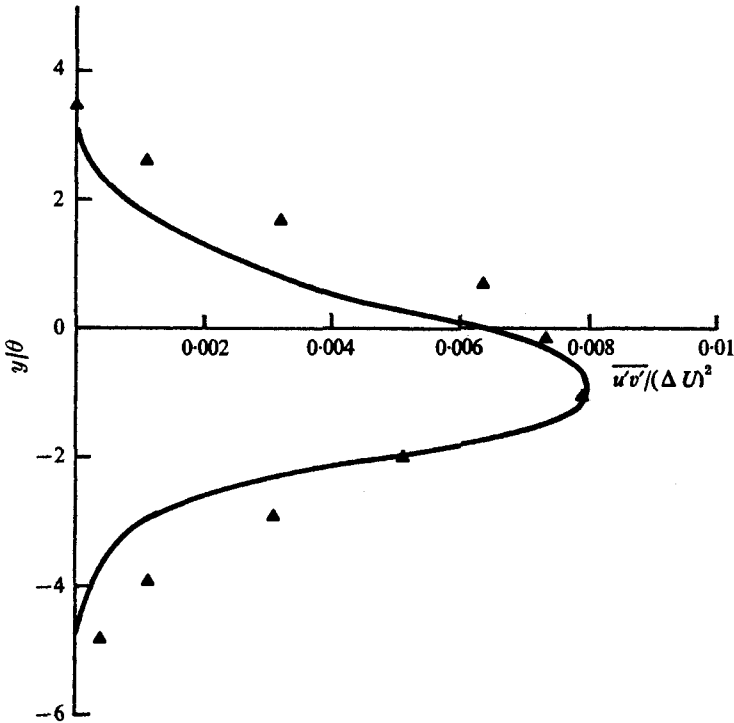
FIGURE 5. Long-time average Reynolds stress, normalized by square of velocity difference ΔU. ▲, present experiment; ———, Liepmann & Laufer (1947).

4. Results and discussion

Time averages and modelling

Conventional time averages define the mean horizontal velocity $\bar{u}(y)$, the root-mean-square fluctuations $\overline{(u'^2)}^{\frac{1}{2}}$ and $\overline{(v'^2)}^{\frac{1}{2}}$, and the Reynolds stress $\overline{u'v'}$ shown in figures 4 and 5. The measurements of mean horizontal velocity and the fluctuations are compared with a flow 'model' to be discussed shortly. The measured Reynolds stress is compared with the earlier experimental results of Liepmann & Laufer (1947).

The distributions of the fluctuations $\overline{(u'^2)}^{\frac{1}{2}}$ and $\overline{(v'^2)}^{\frac{1}{2}}$ across the mixing layer are different from those measured at high Reynolds number. The vertical velocity fluctuation $\overline{(v'^2)}^{\frac{1}{2}}$ is everywhere larger than the longitudinal (horizontal) fluctuation $\overline{(u'^2)}^{\frac{1}{2}}$, and both magnitudes decay rather slowly with distance away from the centre of the mixing layer. Since there is no reason to doubt the accuracy of the measurements (within the bounds discussed earlier), an attempt was made to explain this behaviour by modelling the mixing-layer flow.

The model employs Stuart's exact solution of the inviscid equations consisting of a row of vortical structures having distributed vorticity (Stuart 1967). Two rows of vortices, one row having spacing L and one having spacing $2L$, were allowed to sweep past the measurement point. No interaction between the two

rows occurs: they simply occupy a certain (mutually exclusive) fraction of the time record. Pairing is accounted for by the presence of vortices with two length scales and by allowing the centres of the vortices to be displaced in the vertical direction with some prescribed probability distribution. Thus

$$u_1 = \overline{U} - \tfrac{1}{2}\Delta U \sinh \frac{2\pi(y-y_0)}{L} \bigg/ \left(\cosh \frac{2\pi(y-y_0)}{L} - \alpha \cos \frac{2\pi\overline{U}t}{L} \right), \qquad (1\,a)$$

$$v_1 = +\tfrac{1}{2}\Delta U \sin \frac{2\pi\overline{U}t}{L} \bigg/ \left(\cosh \frac{2\pi(y-y_0)}{L} - \alpha \cos \frac{2\pi\overline{U}t}{L} \right), \qquad (1\,b)$$

$$u_2 = \overline{U} - \tfrac{1}{2}\Delta U \sinh \frac{\pi(y-y_0)}{L} \bigg/ \left(\cosh \frac{\pi(y-y_0)}{L} - \alpha \cos \frac{\pi\overline{U}t}{L} \right), \qquad (1\,c)$$

$$v_2 = +\tfrac{1}{2}\Delta U \sin \frac{\pi\overline{U}t}{L} \bigg/ \left(\cosh \frac{\pi(y-y_0)}{L} - \alpha \cos \frac{\pi\overline{U}t}{L} \right), \qquad (1\,d)$$

where the centres of the vortices are at $y = y_0$, $t = nL/\overline{U}$, $n = 0, 1, 2, \ldots$, and α measures the concentration of vorticity. The instantaneous velocity is

$$u = I(t)u_1 + (1-I(t))u_2, \quad v = I(t)v_1 + (1-I(t))v_2, \qquad (2)$$

where

$$I(t) = 0 \quad \text{or} \quad 1; \quad \frac{1}{T}\int_0^T I(t)\, dt = \gamma.$$

The expected values of the time-averaged properties (an overbar indicates a time average) are given by

$$\left. \begin{aligned} E(\overline{u}(y)) &= \gamma \int p(y_0)\, \overline{u}_1(y,y_0)\, dy_0 + (1-\gamma) \int p(y_0)\, \overline{u}_2(y,y_0)\, dy_0, \\[2mm] E(\overline{u'^2}(y)) &= \gamma \int p(y_0)\, \overline{u_1'^2}(y,y_0)\, dy_0 + (1-\gamma) \int p(y_0)\, \overline{u_2'^2}(y,y_0)\, dy_0, \\[2mm] E(\overline{v'^2}(y)) &= \gamma \int p(y_0)\, \overline{v_1'^2}(y,y_0)\, dy_0 + (1-\gamma) \int p(y_0)\, \overline{v_2'^2}(y,y_0)\, dy_0. \end{aligned} \right\} \qquad (3)$$

Best agreement with measurements is obtained for

$$\alpha = 0.60, \quad L = 1.3\,\text{cm}, \quad \gamma = 0.70,$$

$$p(y_0) = \begin{cases} 1 & \text{for} \quad |y_0/L| \leqslant 0.35, \\ 0 & \text{for} \quad |y_0/L| > 0.35, \end{cases}$$

and these results are shown in figure 4.

The comparison is by no means exact, but the model does reproduce the main feature of the measurements, namely the qualitatively correct ratio of vertical to horizontal fluctuations. The model gives $2L \simeq 2.6\,\text{cm}$ and predicts a value for the momentum thickness θ of $0.237\,\text{cm}$, while measurements show $2L$ to be nearer $3.4\,\text{cm}$ with $\theta = 0.20\,\text{cm}$. The results are most sensitive to the value of α chosen. The value $\alpha = 0.6$ is consistent with the previous observations of Winant & Browand (1974). The influence of the two scales of vortex motion can be seen in the calculated results. The measurements show even more pronounced secondary lobes in $(\overline{u'^2})^{\frac{1}{2}}$ at large values of y/θ, which must also reflect the dual nature of the flow structure. It does not seem possible to match the measured

amplitudes at large y/θ with the present model and still retain a realistic value for the momentum thickness. Interactions between vortices, which have been neglected here, are probably important. (Interaction would be needed to explain the observed asymmetries in $\overline{(u'^2)}^{\frac{1}{2}}$ and $\overline{(v'^2)}^{\frac{1}{2}}$.) It is also likely that vortical structures of larger dimensions resulting from the occasional coalescence of three vortices contribute significantly to the fluctuations at large y/θ.

The Reynolds stress, normalized by the velocity difference across the mixing layer, is shown in figure 5 and, when compared with the experimental results of Liepmann & Laufer (1947), illustrates an interesting feature. The distribution of Reynolds stress in the present, low Reynolds number flow agrees well (apart from the slight broadening) with the high Reynolds number result, although the root-mean-square fluctuations are quite dissimilar. The tentative conclusion is that the process responsible for the production of Reynolds stress (and, hence, for the maintenance of turbulence) is relatively independent of Reynolds number. The interactions of the largest scales of motion must be responsible for the bulk of the Reynolds stress, since it can be only the large-scale features which remain unaffected by large variations in the Reynolds number. In the paragraphs to follow, more evidence will be presented for the importance of the large-scale vortical interactions to the production of Reynolds stress.

Conditionally sampled, ensemble structure

The two ensemble-averaged flow fields substantiate the visual observations and earlier measurements of Winant & Browand (1974). This is most graphically illustrated by a presentation of the z-component vorticity fields for state I and state II; see figures 6(a) and (b). The vorticity distributions were obtained by smoothing the experimentally determined differences $\Delta u_E(y,t)/\Delta y$ and $\Delta v_E(y,t)/\Delta t$ and by replacing time with $x/\overline{U}$. The subscript E indicates ensemble-averaged values. Then

$$\zeta_E(y,x) = \frac{\Delta u_E}{\Delta y}(y, x/\overline{U}) - \frac{\Delta v_E}{\Delta x}(y, x/\overline{U}). \tag{4}$$

The contours of constant vorticity shown in figure 6, normalized by the maximum time-mean vorticity $\overline{\zeta}$, have an estimated error of $\pm 0.1\overline{\zeta}$. This representation is only approximate since the flow field does *not*, in general, consist of fixed structures convected past the probe. The spatial picture is in reality composed of 30 time steps centred about the vertical lines marking the origin in time in figure 6. (A true spatial picture could be obtained by shifting the x location of the measurement probe forwards and backwards from the location of the detector probes, but the work would increase by a factor of 30.) The distortion not accounted for in (4) is estimated by determining the relative displacement of the two vortex centres in figure 6(b) for an interval of 5 time steps. This displacement will not alter the picture qualitatively.

The ensemble-averaged vorticity fields are very non-uniform in space with peak magnitudes which exceed the maximum mean value by about 60–70%. State II clearly shows the two vortices in the process of combining. The horizontal spacing l of the vortical structures near the completion of a pairing can be
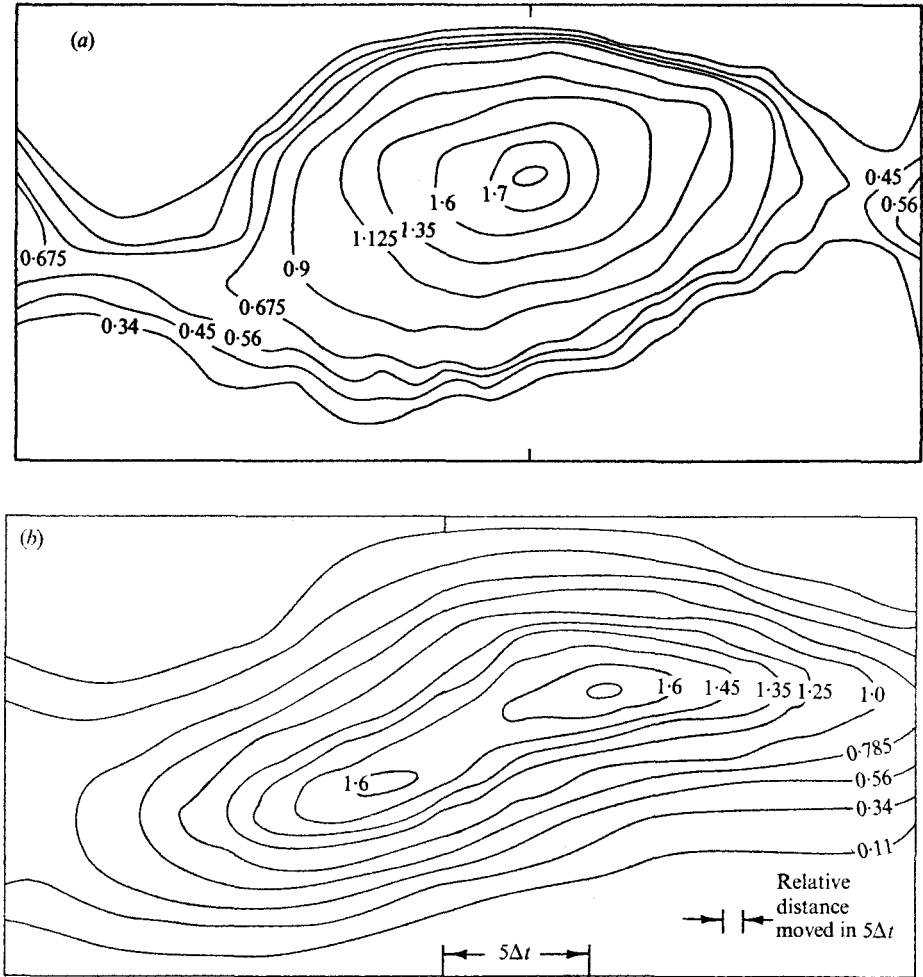
FIGURE 6. Approximate contours of constant vorticity for ensemble-average flow, normalized by maximum time-averaged vorticity $\bar{\zeta} = 2\cdot86\,\mathrm{s}^{-1}$. Vertical mark on boundary corresponds to origin of time samples. (a) State I, final stage in pairing. (b) State II, intermediate stage. The barred length shown at the lower right is the approximate *relative* displacement of the two vortex centres during five time steps $(5\Delta t)$. It is a measure of the error incurred in translating the time sequence (using Taylor's hypothesis) into a spatial vorticity field.

obtained from figure 6(a). The time interval characterizing the pattern is estimated to be 0·9 to 1·0 s (the entire picture is 1·2 s in length), and convecting this pattern with the mean speed gives a value for the spacing of $3\cdot4 \pm 0\cdot2\,\mathrm{cm}$. The vortex spacing is greater than the maximum slope thickness by a factor of about 3·2, in agreement with the observations of Brown & Roshko (1974).

The measured distribution of vorticity in figure 6(a) can be compared with the Stuart vortex (Stuart 1967). Stuart's theoretical distribution is given by

$$\zeta(x, y) = \Delta U l (1 - \alpha^2) \bigg/ \left(\cosh\frac{2\pi y}{l} - \alpha \cos\frac{2\pi x}{l} \right)^2, \qquad (5)$$
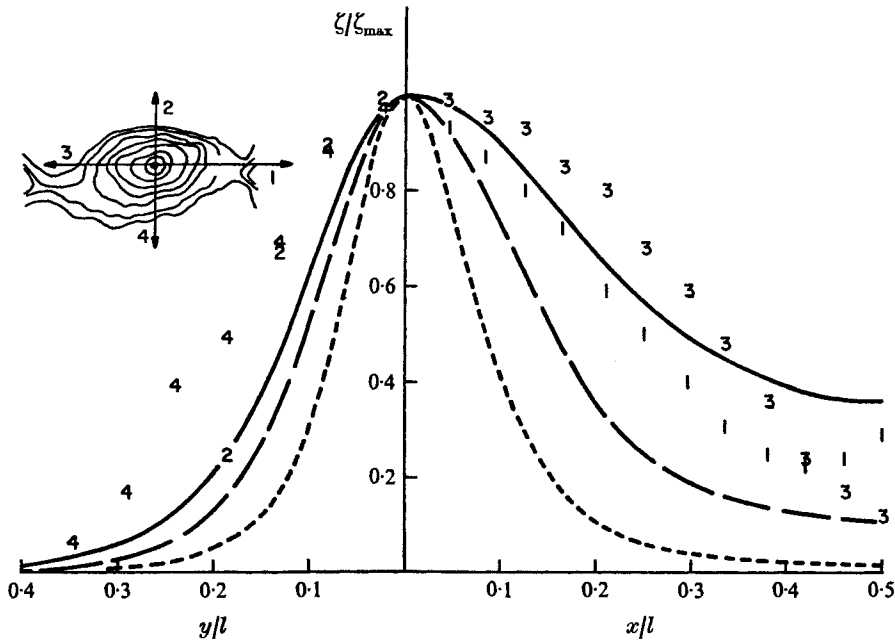
FIGURE 7. Ensemble-averaged vorticity distribution ζ/ζ_{max} for state I compared with Stuart's (1967) exact solution. Numbers indicate co-ordinate directions shown in sketch. Theoretical curves: $\cdots$, $\alpha = 0.75$; ———, $\alpha = 0.5$; ——, $\alpha = 0.25$.

with $x = \bar{U}t$. Choosing the origin of co-ordinates at the point of maximum vorticity ζ_{max} for state I, values of ζ/ζ_{max} are plotted in each of the co-ordinate directions in figure 7. Theoretical curves are presented for three values of α: 0.25, 0.5 and 0.75. The agreement seems only qualitative. The ensemble-averaged vorticity field is broader in y than any of the theoretical curves, and this may be a result of the recent pairing. In the longitudinal direction, there is best overall agreement with a theoretical vortex having $\alpha = 0.25$, although the observed minimum values of vorticity are more characteristic of the $\alpha = 0.5$ result.

Figures 8 and 9 show the ensemble averaged velocity fields for states I and II, respectively. Both u_E and v_E are plotted as departures from the (long) time-averaged values. For state I the vertical velocity field is nearly antisymmetric in time and nearly symmetric in y, while the longitudinal velocity field has the opposite properties. These features suggest simple passive convection for the vortical lumps in state I. On the other hand, the pairing occurring in state II results in a more complicated picture with stronger asymmetry with respect to the time origin.

Additional insight into the relative dynamical importance of state I and state II can be obtained from the measured correlation coefficients computed for each ensemble and averaged in time over the duration of passage; see figures 10(*a*) and (*b*). The correlation coefficient for either state is defined as

$$\overline{u_E' v_E'}/(\overline{u_E'^2})^{\frac{1}{2}}(\overline{v_E'^2})^{\frac{1}{2}},$$
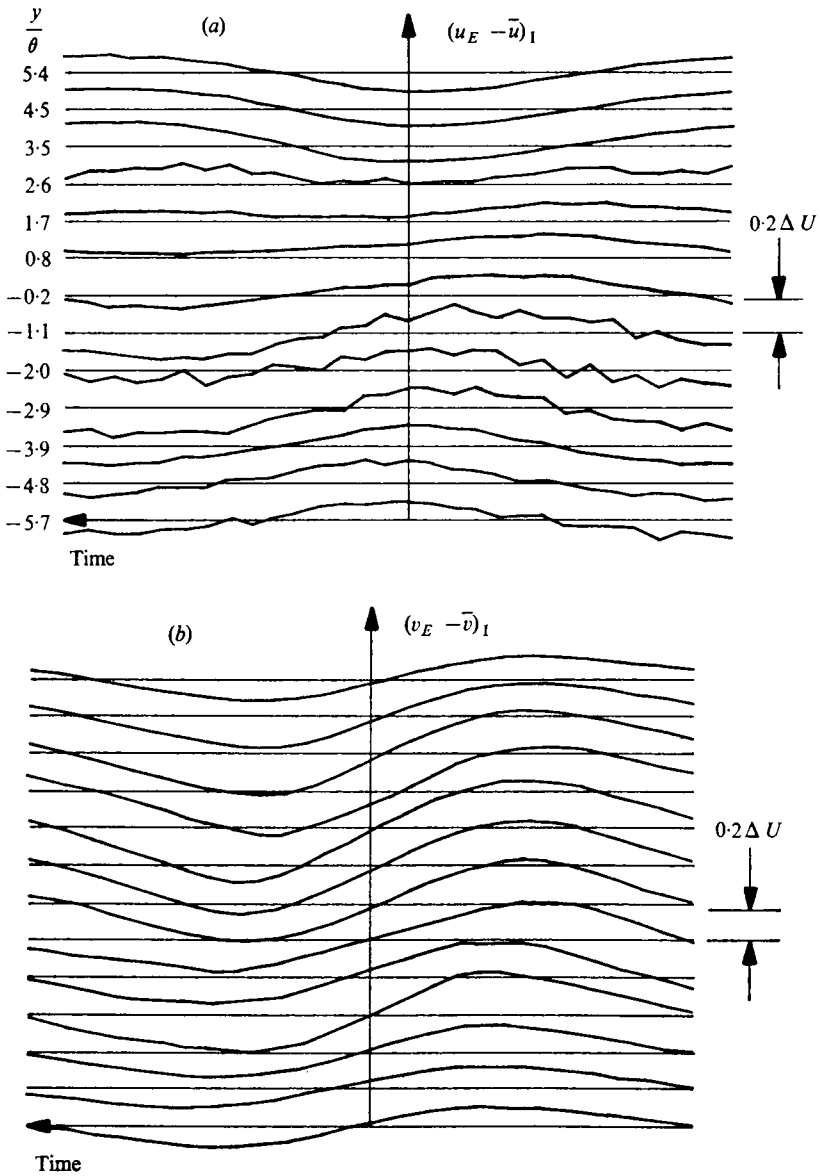
FIGURE 8. Ensemble-averaged velocity field for state I, relative to the time-mean velocity at 13 vertical locations in the mixing layer. (a) Longitudinal velocity. (b) Vertical velocity.

where u_E' and v_E' express the departures of the instantaneous velocity from the ensemble mean values, i.e.

$$u_E'(y, t) = u_E(y, t) - \overline{u_E}(y),$$
$$v_E'(y, t) = v_E(y, t) - \overline{v_E}(y).$$
$$(6)$$

The comparison is made in each case with the experimentally determined, conventional time-averaged correlation coefficient, represented by the dashed curve.
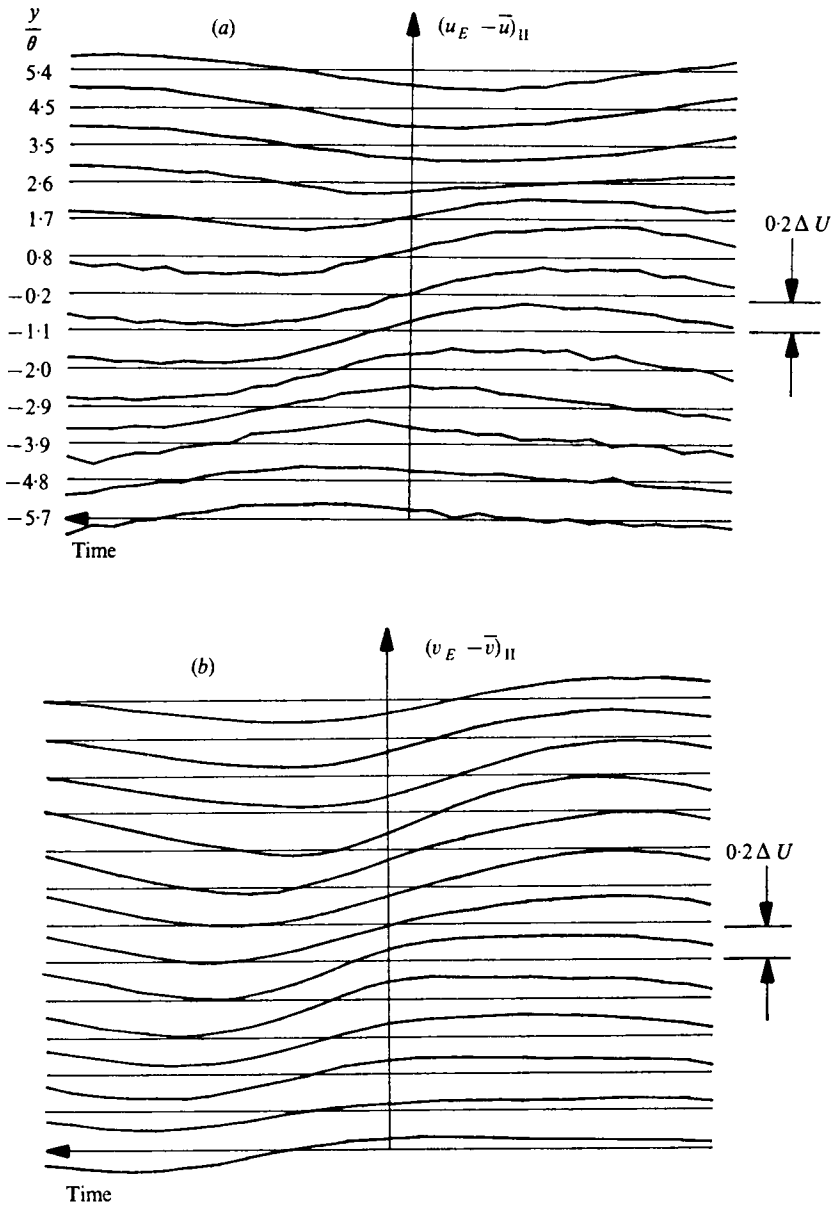
FIGURE 9. Ensemble-averaged velocity for state II, relative to the time-mean velocity at 13 vertical locations in the mixing layer. (a) Longitudinal velocity. (b) Vertical velocity.

Peak values, which exceed the long-time-averaged values, are reached in both states, but the most remarkable correlation occurs during state II. The pairing interaction results in perfect correlation (within experimental accuracy) in a region extending two momentum thicknesses on either side of the point of maximum mean shear.
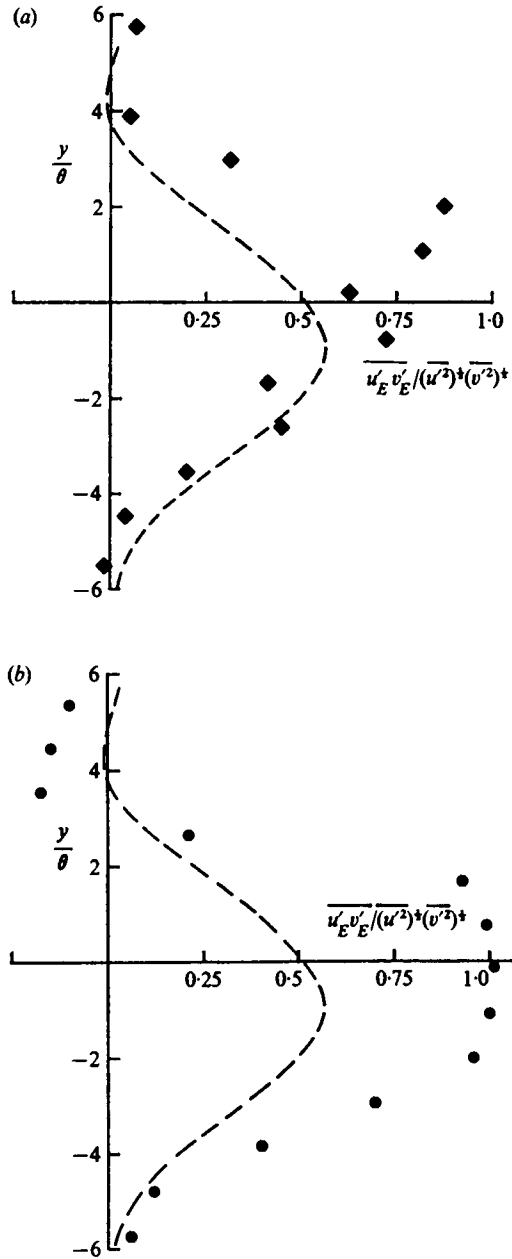
FIGURE 10. Experimentally determined correlation coefficient, averaged over the fraction of time for which either state exists. (*a*) State I. (*b*) State II. Dashed curve is measured long-time averaged correlation coefficient.
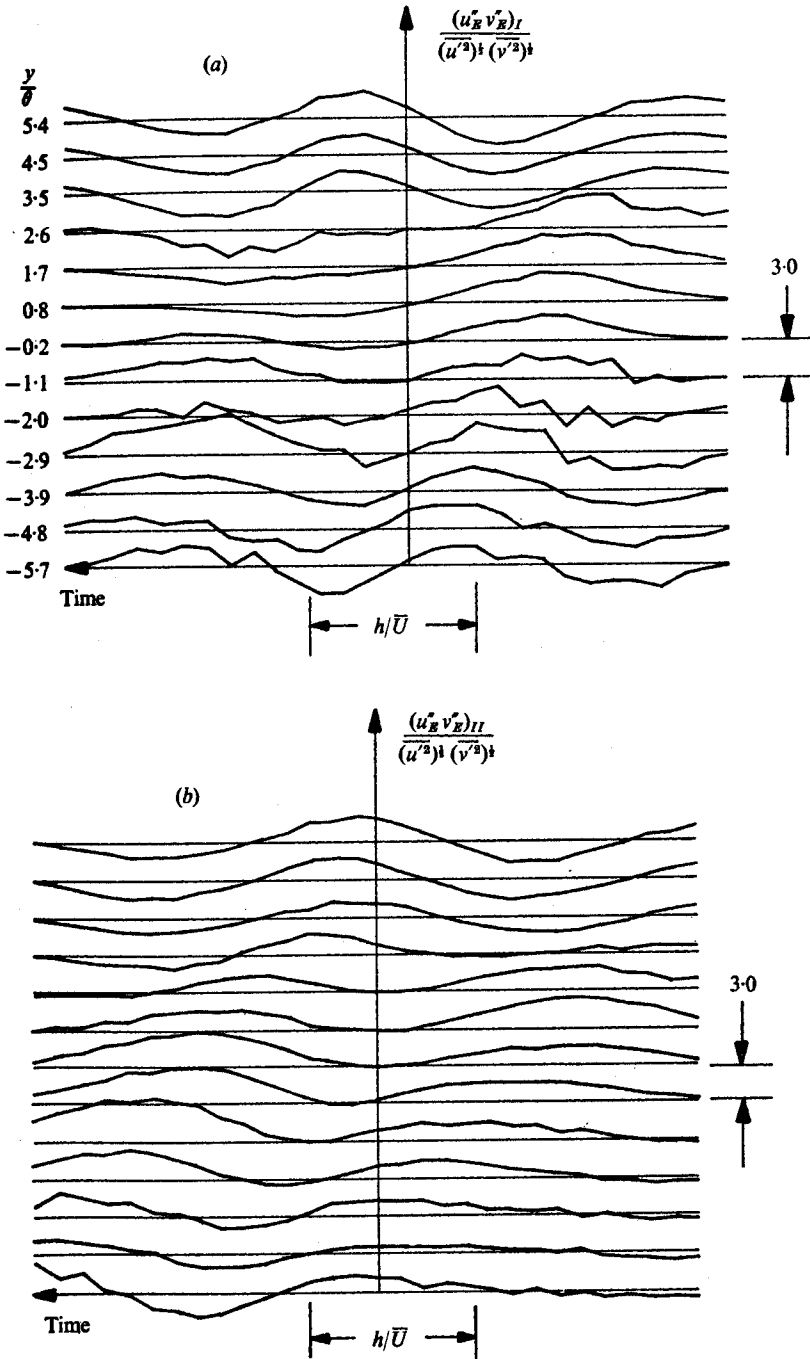
FIGURE 11. Instantaneous momentum transport associated with the ensemble-averaged large-scale flow. (a) State I. (b) State II. The time interval $h/\bar{U}$ is shown at the bottom of the figure.

It is also possible to compare the instantaneous values for states I and II of the product of the ensemble-averaged perturbations,

$$u_E'' v_E'' / \overline{(u'^2)}^{\frac{1}{2}} \, \overline{(v'^2)}^{\frac{1}{2}},$$

shown in figures 11 (*a*) and (*b*). Here, u_E'' and v_E'' are defined slightly differently as the deviations of the instantaneous ensemble velocities from the long-time-mean values, i.e.

$$\left. \begin{aligned} u_E''(y, t) &= u_E(y, t) - \overline{u}(y), \\ v_E''(y, t) &= v_E(y, t) - \overline{v}(y). \end{aligned} \right\} \tag{7}$$

The product $u_E'' v_E''$ can then be identified with the instantaneous momentum flux associated with the large-scale motion. The momentum flux is normalized by the product of the conventional time-averaged fluctuations. The area under any curve in figure 11 – that is, the integral over time – is the contribution to the total Reynolds stress during the fraction of time for which state I or state II exists. It is a measure of the importance of either state to the production of a *net* Reynolds stress. In state I, the tendency towards antisymmetry of the flow field about the time origin produces compensating positive and negative momentum flux contributions. In state II, primarily positive contributions in the central portion of the mixing layer are produced throughout the passage. (In our co-ordinate system, positive Reynolds stress implies perturbation energy gain.) Referring again to figure 9, it can be seen that these positive contributions to the momentum flux come about equally from the upward transport of high momentum fluid, and the downward transport of low momentum fluid.

The magnitude of $u_E'' v_E''$ is never particularly large – it barely exceeds the maximum time-mean value by a factor of five – whereas, in boundary-layer flows, ensemble-averaged momentum fluxes exceed the maximum time-mean value by a factor of ten (Blackwelder & Kaplan 1976). Instantaneous peak values sixty times greater than the time mean have been measured in the boundary layer by (Willmarth & Lu 1972). In the case of the mixing layer, it is not the sudden, high amplitude event which contributes to the Reynolds stress, but, rather, an organized accumulation of significant correlation over a time comparable to the passage of the largest scales. (One might extend this notion to other free shear flows, which also seem to lack the sudden 'bursting' events characteristic of bounded flows.)

We have tended to attach less importance to state I by describing it as 'simple passive convection'. This is not quite true. There is Reynolds stress produced during the passage of state I, and it would be more correct to describe this state as the final phase of the pairing interaction. There is an orderly progression of states which characterize the complete interaction of the vortical lumps. Our conditional averaging has isolated just two of these: one state near the middle of the process and one state near the end of the process. In attempting to ascribe relative importance to one of these, we are really comparing various stages of the same interaction. What can be said on the basis of results presented here is that significant Reynolds stress associated with the large-scale motion is generated during the intermediate stages of the interaction characterized by state II.

There may, indeed, be times – after the completion of one interaction and before the inception of another – when the vortical structures have roughly the same size and spacing over some limited distance. A condition is thus approached for which the Reynolds stress is small. State I represents the approach to this condition. (For a row of equally spaced vortices of equal strength convected past the point of interest, the Reynolds stress evaluated over any integer number of passage periods would be exactly zero owing to the cancelling contributions to the instantaneous momentum flux.)

A characteristic value of the Reynolds stress produced during state I or state II can be obtained by computing an average across the mixing layer. It is 0·32 for state I and 0·62 for state II, compared with 0·24 for the conventional long-time average. An average value for the entire pairing even might be taken as the mean of states I and II, or about 0·5. If it is assumed that pairing is the sole agent responsible for (large-scale) Reynolds-stress production, then pairing must occupy roughly half of the total time record.

5. Summary and concluding remarks

We have described a measurement technique, using conditional sampling, which focuses directly upon the largest scales of motion in the mixing layer. By means of two detector probes placed on opposite sides of the layer, various stages of the large-scale interactions can be isolated. The technique may also work well in other free shear flows which bear at least a generic relation to the mixing layer.

The results of the conditional sampling indicate that Reynolds-stress production is unquestionably associated with the pairing interaction. Net Reynolds-stress production is characterized by significant correlation of momentum-flux contributions over the time of passage of the large scales, rather than by high amplitude, short duration bursts.

The qualitative features of the large-scale structure in the turbulent mixing layer are insensitive to Reynolds number variation over a wide range. This was most convincingly demonstrated by Brown & Roshko (1974). In the present study, the observed similarities in the magnitude and distribution of net Reynolds stress between our results and the work of Liepmann & Laufer (1947) lend support to the belief that pairing or coalescence is, indeed, a universal feature of the turbulent mixing layer. It is felt that an extension of the present technique can be used to explore the high Reynolds number mixing layer to quantify the detailed features of the large-scale interactions.

The attempts at modelling various features of the flow using Stuart vortices were only qualitatively successful. Non-interacting vortices have a very limited usefulness. Numerical models using interacting vortices would seem, however, to have the attributes required of a predictive scheme.

REFERENCES

BLACKWELDER, R. F. & KAPLAN, R. E. 1976 *J. Fluid Mech.* **76**, 89.

BROWN, G. L. & ROSHKO, A. 1971 The effect of density differences on the turbulent mixing layer. *Turbulent Shear Flows, AGARD Current Paper*, no. 93, 23.1–23.12.

BROWN, G. L. & ROSHKO, A. 1974 On density effects in turbulent mixing layers. *J. Fluid Mech.* **64**, 775.

KIM, H. T., KLINE, S. J. & REYNOLDS, W. C. 1971 The production of turbulence near a smooth wall in a turbulent boundary layer. *J. Fluid Mech.* **50**, 133.

KLINE, S. J., REYNOLDS, W. C., SCHRAUB, F. A. & RUNSTADLER, P. W. 1967 The structure of turbulent boundary layers. *J. Fluid Mech.* **30**, 741.

LIEPMANN, H. W. & LAUFER, J. 1947 Investigation of free turbulent mixing. *N.A.C.A. Tech. Note*, no. 1257.

STUART, J. T. 1967 On finite amplitude oscillations in laminar mixing layers. *J. Fluid Mech.* **29**, 417.

TOWNSEND, A. A. 1956 *The Structure of Turbulent Shear Flow*. Cambridge University Press.

WILLMARTH, W. W. & LU, S. S. 1972 Structure of the Reynolds stress near the wall. *J. Fluid Mech.* **55**, 65.

WINANT, C. D. & BROWAND, F. K. 1974 Vortex pairing: the mechanism of turbulent mixing layer growth at moderate Reynolds number. *J. Fluid Mech.* **63**, 237.
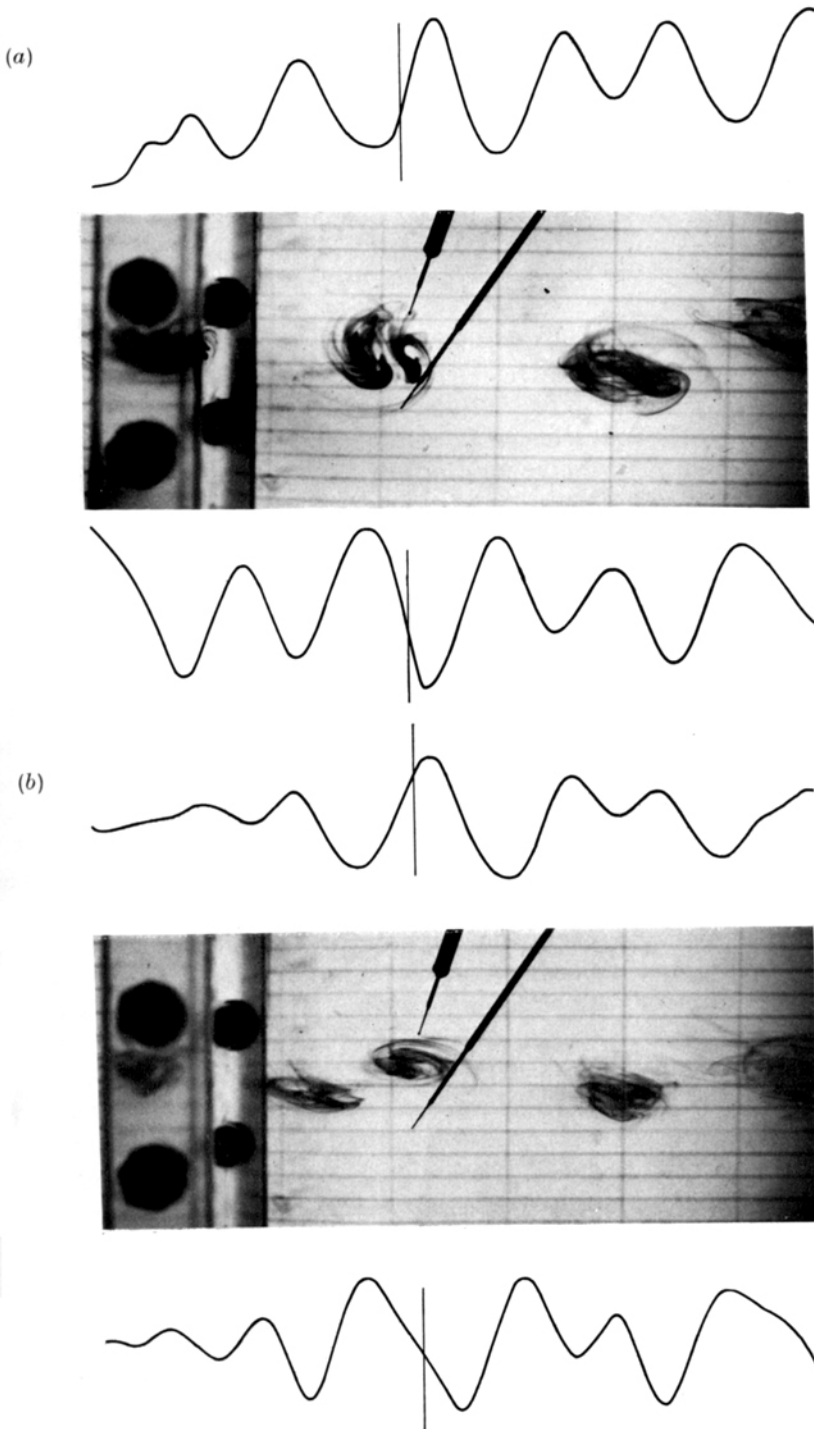
FIGURE 3. Photographs of mixing layer with traces of hot-film outputs. Vertical bars indicate the time of the photograph. Flow is from left to right with lower layer faster. Dye is continuously injected into the boundary layer on the upstream splitter plate. (*a*) Final stage in vortex pairing (the portions comprising the two original vortices are visible). (*b*) Inter-mediate stage in vortex pairing.